

## Simulating drainage and imbibition experiments in a high-porosity micromodel using an unstructured pore network model

V. Joekar Niasar,<sup>1</sup> S. M. Hassanizadeh,<sup>1</sup> L. J. Pyrak-Nolte,<sup>2</sup> and C. Berentsen<sup>1,3</sup>

Received 8 November 2007; revised 27 November 2008; accepted 16 December 2008; published 25 February 2009.

[1] Development of pore network models based on detailed topological data of the pore space is essential for predicting multiphase flow in porous media. In this work, an unstructured pore network model has been developed to simulate a set of drainage and imbibition laboratory experiments performed on a two-dimensional micromodel. We used a pixel-based distance transform to determine medial pixels of the void domain of micromodel. This process provides an assembly of medial pixels with assigned local widths that simulates the topology of the porous medium. Using this pore network model, the capillary pressure-saturation and capillary pressure-interfacial area curves measured in the laboratory under static conditions were simulated. On the basis of several imbibition cycles, a surface of capillary pressure, saturation and interfacial area was produced. The pore network model was able to reproduce the distribution of the fluids as observed in the micromodel experiments. We have shown the utility of this simple pore network approach for capturing the topology and geometry of the micromodel pore structure.

**Citation:** Joekar Niasar, V., S. M. Hassanizadeh, L. J. Pyrak-Nolte, and C. Berentsen (2009), Simulating drainage and imbibition experiments in a high-porosity micromodel using an unstructured pore network model, *Water Resour. Res.*, 45, W02430, doi:10.1029/2007WR006641.

### 1. Introduction

[2] Pore network models have been developed extensively since Fatt [1956] introduced them for modeling capillary pressure-saturation ( $P_c$ - $S$ ) curves. They have been used not only for theoretical studies [see, e.g., Reeves and Celia, 1996; Held and Celia, 2001; Dias and Payatakes, 1986], but also to estimate or predict characteristics of soils and rocks [see, e.g., Blunt et al., 2002; Piri and Blunt, 2005a, 2005b; Valvatne and Blunt, 2004]. For example, Blunt et al. [2002] have suggested that using appropriate pore-scale physics combined with a geologically representative description of the pore space, one can produce capillary pressure and relative permeability curves for a given rock without actual measurements. Vogel [1997, 2000] and Vogel and Roth [1998] have stated that to have a predictive representative pore network model, an accurate translation of topology from the pore space geometry to a pore network is essential. Information on topology of porous samples can be obtained from imaging techniques such as X-ray tomography and microtomography [see, e.g., Montemagno and Pyrak-Nolte, 1995; Coles et al., 1998; Lindquist et al., 2000; Lindquist, 2002; Culligan et al., 2004, 2006; Al-Raoush and Willson, 2005a, 2005b; Wildenschild et al., 2002; Knackstedt et al., 2004], laser confocal microscopy [Fredrich et al., 1993, 1995; Montoto

et al., 1995], and serial sectioning imaging [Vogel, 1997]. Translation of information from such techniques to a pore network model can be done in two different ways; statistically representative models and topologically representative models. Statistically representative models capture the statistical distribution of pore size and connectivity and not the exact topology of the pores. They are usually in a structured lattice, and pore bodies and pore throat distributions are determined so that on a REV scale they represent a real porous medium. In these statistically representative models, information acquired from imaging techniques is used to construct a network of pore bodies connected by pore throats. Pore bodies and pore throats are assigned regular geometrical shapes amenable to simple flow analysis. This translation of information, however, is not straight forward. Often many idealizations of the pore size, shape, and orientation are used. Topologically representative models are also based on detailed data provided by imaging techniques that include connectivity, position and orientation of pore bodies and pore throats. Thus, more detailed simulations are possible using these topologically representative models. Therefore, it is desirable to develop an approach that transforms the real geometry of the porous medium to a pore network with minimum loss of information, yet allows the computation of distribution of fluids within the network in a fairly simple way.

[3] One of the approaches for constructing the pore geometry from the imaging data is medial axis transform and skeletonization. Computationally, there are two general methods to find the medial axis of a given geometry: pixel-based and pixel-free methods [see, e.g., Montanari, 1969; Brady and Asada, 1984; Saint-Marc et al., 1993; Chang et al., 1999]. One may say that pixel-free methods are more

<sup>1</sup>Department of Earth Sciences, Utrecht University, Utrecht, Netherlands.

<sup>2</sup>Department of Physics, Purdue University, West Lafayette, Indiana, USA.

<sup>3</sup>Now at Department of Geotechnology, Technical University of Delft, Delft, Netherlands.

precise than pixel-based methods since their computations are not implemented in a discrete domain. However, these methods also use pixelized input data acquired from imaging techniques that require approximations in order to transform the data into polyhedrons and lines. In these methods, midpoints or center lines of the pairs of contour elements bounding a shape are calculated analytically and are connected to generate the skeleton of a given geometry. Compared to pixel-free ones, pixel-based methods are usually simpler and easier to implement. However, since they are implemented on a discrete domain, they are not guaranteed to follow the exact medial axis. For skeletonization and finding medial axis, one may use different algorithms such as thinning algorithm [Smith, 1987; Lam and Lee, 1992], distance transformation, DT [introduced by Rosenfeld and Pfalz, 1968], and medial axis transform, MAT [introduced by Blum, 1967]. Most of the existing pixel-based skeletonization methods use thinning techniques [Lam and Lee, 1992], which have been used extensively in many applications in biology, X-ray image analysis, finger print analysis, qualitative metallography, soil cracking pattern, automatic analysis of industrial parts as well as porous media [Lam and Lee, 1992]. Distance transform has also many important applications in expanding or shrinking objects, reconstructing objects from parts of a given boundary [Matsuyama and Phillips, 1984] as well as for computing Voronoi diagrams [Ye, 1988; Ogniewicz and Ilg, 1992]. MAT methods have been used for computing many geometric properties [Lee, 1982; Chandran et al., 1992; Wu et al., 1986, 1988]. In fields related to porous media, some researchers such as Lindquist [2002] and Glantz and Hilpert [2007, 2008] have employed medial axis transform concept to extract topology and geometry of a porous medium. Glantz and Hilpert [2007] have applied their pixel-free approach to simulate a drainage experiment on a two-dimensional porous medium composed of circular grains. Subsequently, they simulated the  $P_c$ - $S$  curve for a drainage experiment in a three-dimensional space porous medium [Glantz and Hilpert, 2008].

[4] In this work, we use a pixel-based method to develop an unstructured pore network model to simulate micromodel experiments performed by Cheng [2002]. Their micromodel had a porosity >66% and had irregular pore geometry. Porous media with high porosities (40% to 98%) are found in many industrial applications such as metallic thin-fiber material and metallic powder, which are used in the transportation industry [Dubikovskaya et al., 1990], and in manufacturing capillary structures [Reimbrecht et al., 2003]. Because of these special features of the micromodel, conventional pore network models with pore body and pore throat elements are not suitable. Thus, we have employed the medial pixel concept to extract the skeleton of the micromodel. We have used a pixelized distance transform to identify the medial pixels and the pore width at every pixel. As a result, the real pore geometry and topology is captured without losing significant information. With our pore network mode, we have simulated a set of quasi-static drainage and imbibition laboratory experiments performed on a two-dimensional porous micromodel porous [Cheng et al., 2004]. We demonstrate the capabilities of the model by simulating fluid configurations observed in the micromodel as well as by calculating capillary pressure-saturation ( $P_c$ - $S$ )

and interfacial area-saturation ( $a_{nw} - S$ ) curves that agree well with the measured data. A  $P_c$ - $S$ - $a_{nw}$  surface for imbibition cycles also agreed with the experimental data.

## 2. Material and Experiment

[5] Cheng [2002] and Cheng et al. [2004] performed fluid invasion experiments on two-dimensional micromodels with random pore structures. Details of the fabrication procedure and the experiments can be found in Cheng [2002]. The main objective of the Cheng [2002] and Cheng et al. [2004] micromodel experiments was to investigate the conjecture of Hassanzadeh and Gray [1990] that capillary pressure ( $P_c$ ) is not only a function of saturation ( $S_w$ ), but also of interfacial area between the nonwetting and wetting phases ( $a_{nw}$ ). Their work provided experimental support for the theoretical prediction that the capillary-dominated subset plays a role analogous to a state variable. The goal of our study is to use pore network modeling to reproduce the fluid distributions and the  $P_c$ - $S$ - $a_{nw}$  relationship observed in their experiments based on the pore geometry of the micromodels.

[6] The micromodel measured approximately  $600 \mu\text{m} \times 600 \mu\text{m}$  with a constant depth of  $1.28 \mu\text{m}$  (Figure 2). The pores had a rectangular cross section of variable width but with a constant height. The porosity of the porous medium was around 62–64%. The micromodel was completely transparent which enabled direct visualization and imaging of fluid distributions within the pores using a microscope with a 16x objective and a CCD camera. From the images of the micromodel, fluid saturation, interfacial area and interfacial curvature were determined. During the experiments, the micromodel was placed horizontally on a microscope to avoid gravitational effects. An external pressure transducer was used to measure the nonwetting phase (nitrogen) pressure. The wetting phase (decane) reservoir was open to atmosphere. In the two-phase displacement experiments of Cheng et al. [2004], nitrogen was used as the nonwetting phase and decane as the wetting phase. The contact angle of the wetting phase with the glass is  $4.4^\circ$  and with the photoresist material is  $4.1^\circ$ . The fluid-fluid interfacial tension is 24.7 dynes/cm. Images of fluid distributions in the micromodel were recorded for drainage and imbibition cycles.

[7] At the start of a drainage experiment, the micromodel was saturated with the wetting phase (decane). Nonwetting phase (nitrogen) was injected into the model by manually increasing the nitrogen pressure in small increments to avoid sudden flooding of the micromodel. At each pressure step, the system was allowed to equilibrate. Then, an image and pressure reading were taken. A drainage experiment was continued until nitrogen gas reached the wetting reservoir. Contrary to standard capillary pressure cells, there was no hydrophilic membrane placed at the exit. So, the nonwetting phase entered the wetting reservoir (break-through) at which time the drainage experiment was halted. At the end of drainage test, there was still a significant amount of the wetting phase present in the micromodel. Then, an imbibition experiment was performed by reducing the nonwetting phase pressure in small increments and at each pressure step allowing the system to equilibrate. The imbibition experiment was continued until the micromodel was almost 100% saturated with the wetting phase. An archive of the images from the Cheng et al. [2004] experiments and other micromodel experiments [Chen et al.,

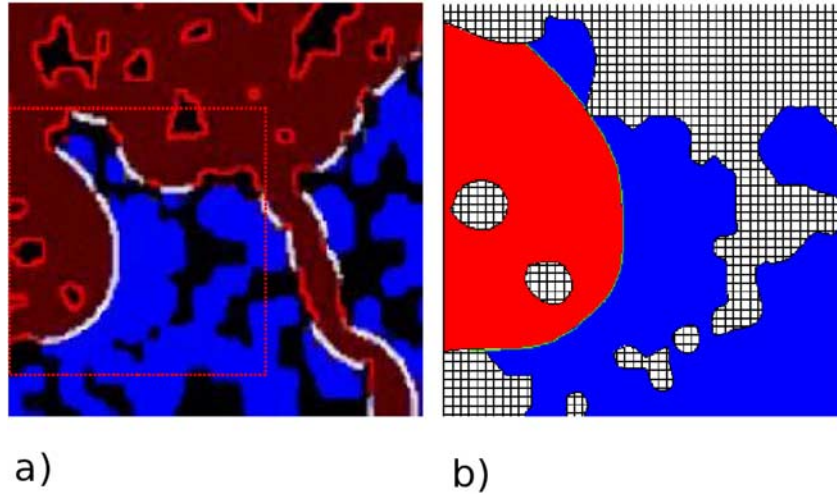


**Figure 1.** An example of cooperative pore filling during imbibition (blue is wetting fluid, red is nonwetting fluid, hashed is the solid). (a) An image of micromodel experiment. (b) Schematic presentation of cooperative-filling interface.

2007; Pyrak-Nolte et al., 2008] have been placed on a Web site for downloading (L. J. Pyrak-Nolte, 2007, <http://www.physics.purdue.edu/rockphys/DataImages/>).

[8] On the basis of images of the experiments, fluid configurations during imbibition were more complicated than those observed from the drainage experiments. At the end of an imbibition experiment, no nonwetting fluid remained in the micromodel. This suggests that trapping mechanisms were absent in this system. In particular, fluid movement should have been piston-like with no snap-off occurring. However, images from imbibition experiments showed that cooperative filling of the pores by the wetting phase was the dominant pore-filling mechanism in this micromodel pore structure. The image in Figure 1 shows an example of cooperative filling in the micromodel. During imbibition, the wetting-nonwetting interface spanned several pores, whereas during drainage, the interfaces moved in individual pores.

### 3. Pore Network Model Description

[9] To develop an unstructured pore network, a binary image of the air-filled micromodel is used. In the image, the pore space (void domain) and its boundaries (solid domain) are visible with a resolution of  $0.6 \mu\text{m}$  per pixel (Figure 2a). The skeleton of the micromodel, and the local pore width are needed to simulate the pore geometry. We have developed a pore network model using a pixel-based distance transform to identify the medial pixels of pores, i.e., the pixels along the center of the channels that are equidistant from the pore channel walls. This approach is relatively simple compared to pixel-free methods.

#### 3.1. Determination of Medial Pixels

[10] We used a Distance Transform, **DT**, to generate a distance map from a binary image of the micromodel. Each

pixel in the void domain was given a value indicating the shortest distance to the solid pixels (pore walls). Then, the value of each pixel was compared to the value of the neighboring pixels. A so-called flow operator [Jensen and Domingue, 1988] was applied to define the direction of the maximum gradient in a two-dimensional space. A search algorithm was used to identify the medial pixels. A detailed explanation of the algorithm is given in Appendix A and an example of the procedure is shown in Figure 2b.

#### 3.2. Determination of Fluids Distribution

[11] Our goal was to obtain the same fluids distributions using our pore network model as those observed in the micromodel. The fluids distribution is dictated by fluid pressures imposed on the model, the equilibrium of capillary forces within the pores, and the history of the displacement. During drainage, only those pores with entry capillary pressures smaller than the imposed capillary pressure were invaded by the nonwetting phase. The entry pressure varies among the pores because the pores in the micromodel have variable cross sections. Therefore, an entry pressure was calculated for each cross sections for all of the pores.

[12] The entry pressure depends on the fluid-fluid interfacial tension ( $\sigma_{nw}$ ), the pore size, pore geometry, and the contact angle ( $\theta$ ). As shown in Figure 3, the pores in the micromodel have a rectangular cross section, and their boundary is partly glass and partly photoresist material. We denote the depth of the micromodel by “a” and the pore width by “b”. Because the difference between the contact angles of the fluid-glass and of fluid-photoresist is insignificant ( $\sim 0.3^\circ$ ), we employ a single value of contact angle in our calculations. The entry pressure,  $P_e$ , for a pore with rectangular cross section is calculated from the following formula which is derived in Appendix B:

$$P_e = \sigma_{nw} \left( \frac{-(a+b) \cos \theta + \sqrt{(a+b)^2 \cos^2 \theta + 4ab \left( \frac{\pi}{4} - \theta - \sqrt{2} \cos \left( \frac{\pi}{4} + \theta \right) \cos \theta \right)}}{4 \left( \frac{\pi}{4} - \theta - \sqrt{2} \cos \left( \frac{\pi}{4} + \theta \right) \cos \theta \right)} \right)^{-1} \quad (1)$$

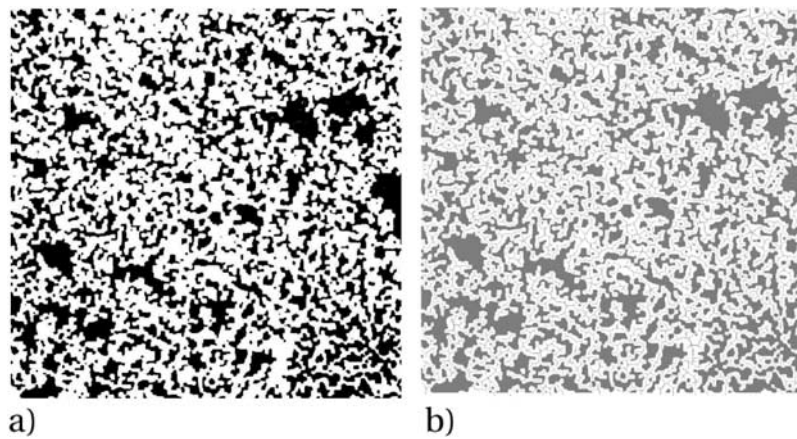


**Figure 2.** (a) Pattern of the micromodel; black shows the solid. (b) Pore network model representation as an assembly of the medial pixels (1 pixel  $\approx 0.3 \mu\text{m}$ ).

Thus, for a given  $P_c$  imposed on the micromodel, the fluid-fluid interface advances to all cross sections with an entry pressure less than  $P_c$  (i.e.,  $P_e \leq P_c$ ), provided the pore is connected to the wetting phase reservoir. If the interface reaches a diverging cross section, the rest of the pore will be filled up by the nonwetting phase. However, for a (partially) converging pore, the interface will stop at the location where the corresponding  $P_e$  is equal to  $P_c$ . It will only move farther after  $P_c$  is increased again. When the location of the interface is known, a local pore width is used to determine the planar arc length of the interface. Because the depth of the micromodel is constant, the interfacial area of the main terminal interface is simply the arc length times the micromodel depth. For imbibition, the reverse occurs. The wetting phase will reenter smallest pores first. In a diverging pore, the meniscus will stop at a location whose local  $P_e$  is equal to  $P_c$ . Converging pores will be completely filled at once.

### 3.3. Trapping Assumptions

[13] In determining the displacement of one phase by another, we must take into account that we may have trapping of the wetting phase during drainage and trapping

of the nonwetting phase during imbibition. In general, during drainage, trapping can occur in two ways. First, wetting phase always exists in the corners of a pore and the amount of wetting phase in the corners will decrease if  $P_c$  is increased and if the corners are connected to the wetting reservoir. For this type of trapping, there is always an interface in the crevices called “corner meniscus”. The second type of trapping is caused by the blockage of some pores. In this case, an interface spans the pore cross section, and it is called a “main terminal meniscus” [Piri and Blunt, 2005a]. Because of the two-dimensionality of the micromodel and the resolution of images, only the second-type of trapping is visible. The corner menisci are not observed in the images and cannot be quantified from the images. Therefore, to simulate the analysis of the experiments performed by Cheng *et al.* [2004], our calculations do not take into account the wetting phase in the corners of the rectangular pores nor the interfacial area of the corner menisci.

[14] Trapping of main terminal menisci can have a significant effect on fluids distribution and consequently on the interfacial area-saturation ( $a_{nw}$ - $S$ ) relationship [see,

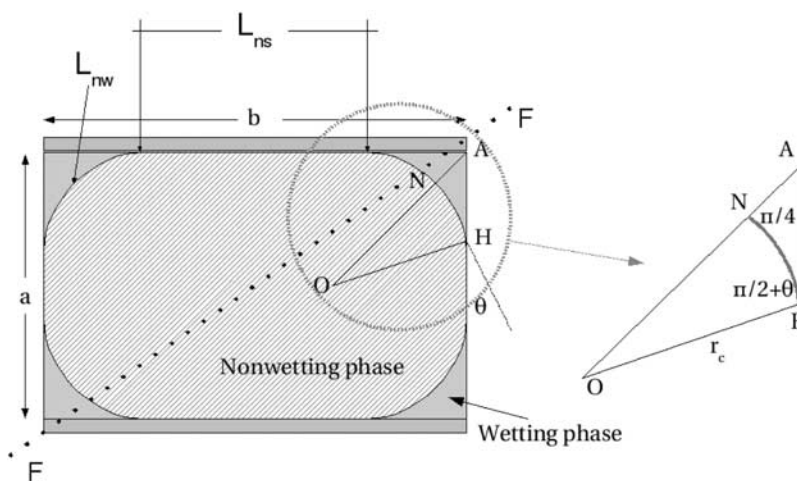


**Figure 3.** Configuration of a meniscus in the corners of a rectangular pore. The variable  $a$  is the depth of micromodel and  $b$  is the local pore width. Half of a corner meniscus with  $r_c$  radius of curvature has been magnified in the right side. Total length of contact line between solid and nonwetting phase is denoted by  $L_{ns}$ , and total length of contact line between nonwetting phase and wetting phase is referred to as  $L_{nw}$ .

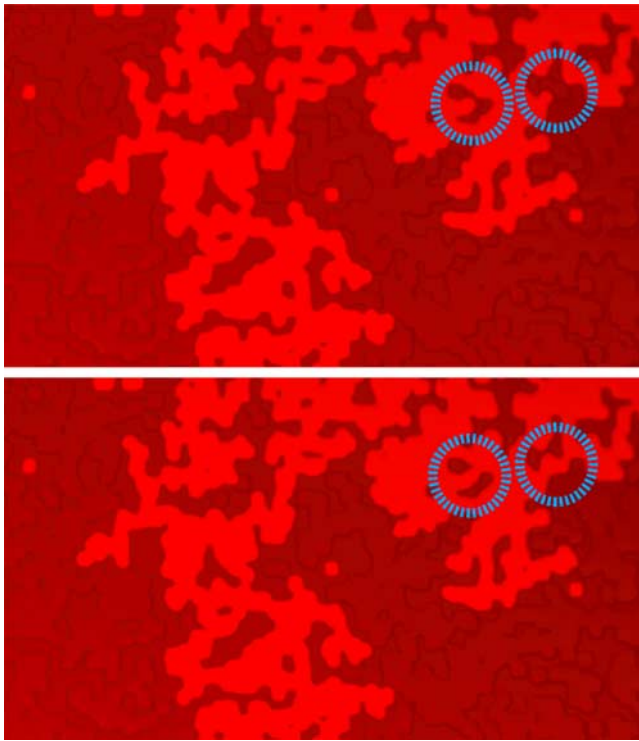


**Figure 4.** Reconnection of main terminal interfaces due to untrapped conditions. Two successive images during drainage experiment show that interfacial area can decrease due to the interfaces reconnection.

e.g., Joekar-Niasar et al., 2008]. The trapping assumptions made for simulations of drainage and imbibition experiments are discussed separately. For drainage experiments, we can consider two different possibilities. One possibility is to assume that the wetting phase is never trapped. This can be justified based on the fact that the wetting phase, which always remains present in the corners of pores, provides a continuous path for the wetting phase to escape to its corresponding reservoir. This means that the wetting phase can be fully drained from all pores if the imposed capillary pressure is sufficiently high. Another possibility is to assume that the wetting-phase-filled corners of the pores do not act as conduits for the flow of the wetting phase. In this case, we can assume that the wetting phase gets trapped in pores that are not connected to the wetting phase reservoir through other (partially) filled pores. Joekar-Niasar et al. [2008] have shown that the shape of  $a_{nw}$ - $S$  curve (calculated based on main menisci interface) is dictated by the trapping assumptions. A monotonic increase of interfacial area, with a decrease in saturation will be obtained if we allow trapping of main terminal menisci. A nonmonotonic  $a_{nw}$ - $S$  curve, however, is found if we impose a loose or no trapping mechanism. This occurs because some main terminal interfaces will be reconnected. Such a reconnection has been observed in the experiments, as illustrated in Figure 4, which shows fluid configurations at two different pressures during the drainage experiment. On the basis of this observation, no trapping of the wetting phase is assumed in our simulations. But, to illustrate the effect of the trapping assumption, one of the drainage simulations has been shown with a simple trapping rule. On the basis of this rule, the wetting phase in a cell of the pore network is

trapped if there is no neighboring cell filled with the wetting phase and connected to the wetting phase reservoir.

[15] Trapping mechanisms during imbibition are different and more complicated compared to those that occur during drainage. Previous studies have shown that displacement mechanisms during imbibition may be attributed to the following factors: (1) pore size distribution, (2) fluid occupancy in pore throats connected to a pore body, and/or (3) pore throat to pore body diameter ratio. Lenormand and Zarcone [1983, 1984] have suggested different mechanisms for imbibition into a pore body that depends on the fluid topology of the neighboring pore throats. According to Wardlaw and Yu [1988] and Ioannidis et al. [1991], little variability of pore size, and small pore body to pore throat diameter ratio are factors that increase the effects of fluid topology in determining the nonwetting phase withdrawal sequence. Such local geometrical features result in a mechanism called cooperative filling. Figure 5 shows a schematic of interface configurations subjected to cooperative pore filling for two different cases. When the ratio of pore body to pore throat diameter is large (small pore throats), interfaces remain within a pore body. However, when the ratio of pore body to pore throat diameter is small, imbibition phenomena are controlled by the fluid topology, and the efficiency of wetting invasion increases significantly [Vidales et al., 1998; Mahmud and Nguyen, 2006] and the effect of snap-off decreases. As observed in the micromodel experiments, there is no trapping at the end of the imbibition experiments. We conclude that snap-off is absent in the experiments and is not one of the major mechanisms of trapping of nonwetting phase [Chatzis and Dullien, 1981]. Absence of snap-off occurs when the pore body to pore throat diameter ratio is small which results in an interface that bridges over several pores. This results in a large radius of curvature and consequently a low capillary pressure. The interface will maintain a stable position as well as continuity to the nonwetting phase reservoir until the global capillary pressure during imbibition is reduced enough to allow invasion of wetting phase. Thus in cooperative filling, a low capillary pressure is required for the wetting phase to fill the pore body completely.

[16] It is difficult and computationally expensive to capture the geometry of interfaces based on a cooperative

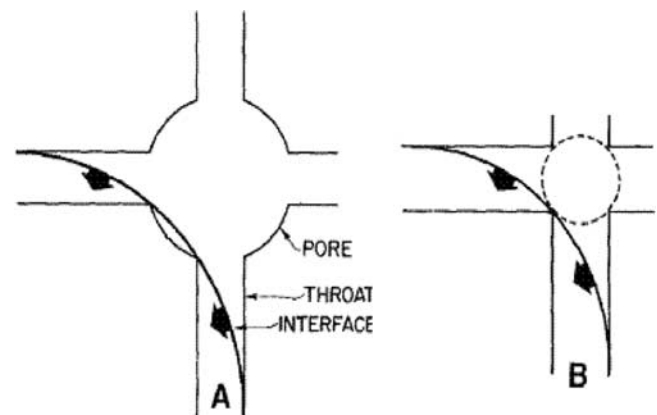


**Figure 5.** Interfaces at positions of break-off in the pores with different pore to throat diameter ratios; (a) Larger ratio. (b) Smaller ratio [Wardlaw and Yu, 1988] (with kind permission from Springer Science+Business Media).

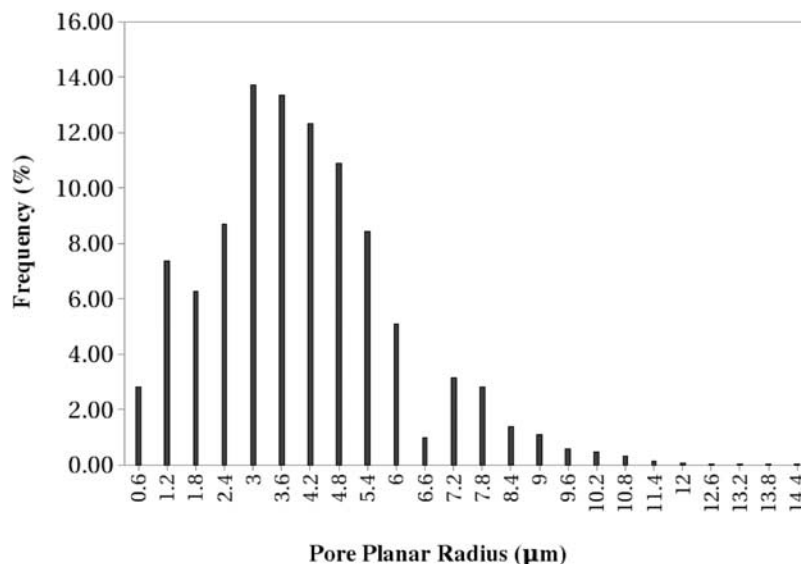


**Figure 6.** Statistical distribution of radii of inscribed circles (half width of pore) of the network model.

filling mechanism when using a skeleton-based pore network model. Thus, cooperative filling has not been modeled explicitly. However, its effect (namely, the decrease in residual nonwetting saturation) has been incorporated in the model using a local network rule, referred to as forced displacement. This rule allows invasion of the wetting phase into a pore as long as it does not break the continuity of the nonwetting phase connection to the nonwetting phase reservoir (i.e., no snap-off occurs during imbibition).

### 3.4. Simulation of Experiments

[17] The numerical analysis started with drainage simulations because the micromodels in the experiments were initially saturated with wetting phase. The wetting phase pressure was assumed to be zero in the entire pore network.

Initially, the pressure of the nonwetting phase, and thus the network capillary pressure, was set equal to the entry capillary pressure of the largest pore(s) bordering the nonwetting phase reservoir. Then, the nonwetting phase pressure was increased incrementally. At each increment, only those pores connected to the nonwetting phase reservoir are invaded if their entry pressure was smaller than or equal to the imposed capillary pressure. At each displacement, saturation and specific interfacial area were calculated.

[18] Drainage simulations were halted after the breakthrough of the nonwetting phase. Then, imbibition experiments were simulated by decreasing the nonwetting phase pressure in small steps. Imbibition always started from the smallest pores with the highest entry capillary pressure. At each imbibition step, the forced displacement rule was

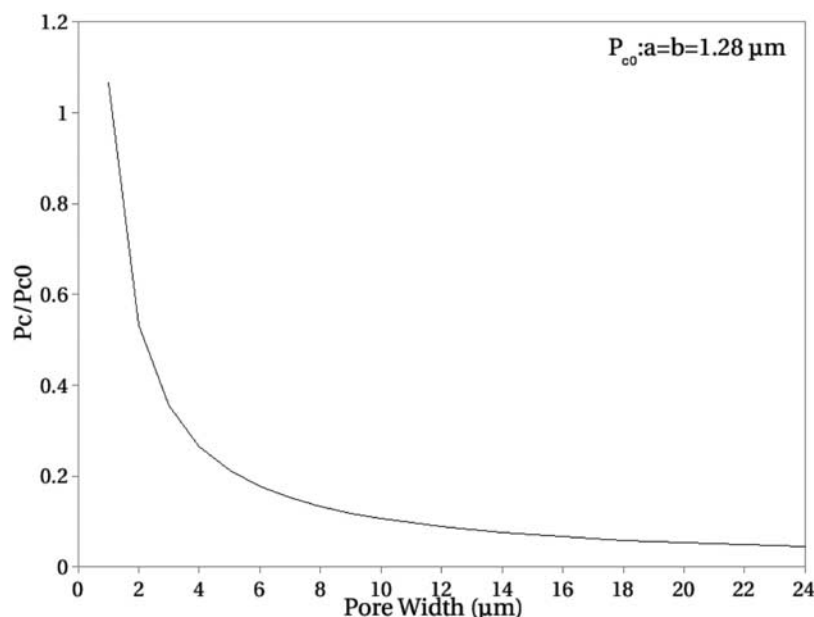


**Figure 7.** Entry capillary pressure for a rectangular cross section as a function of pore width, normalized with respect to  $P_{c0}$ , which is the entry capillary pressure for a pore with  $a = b = 1.28 \mu\text{m}$ .

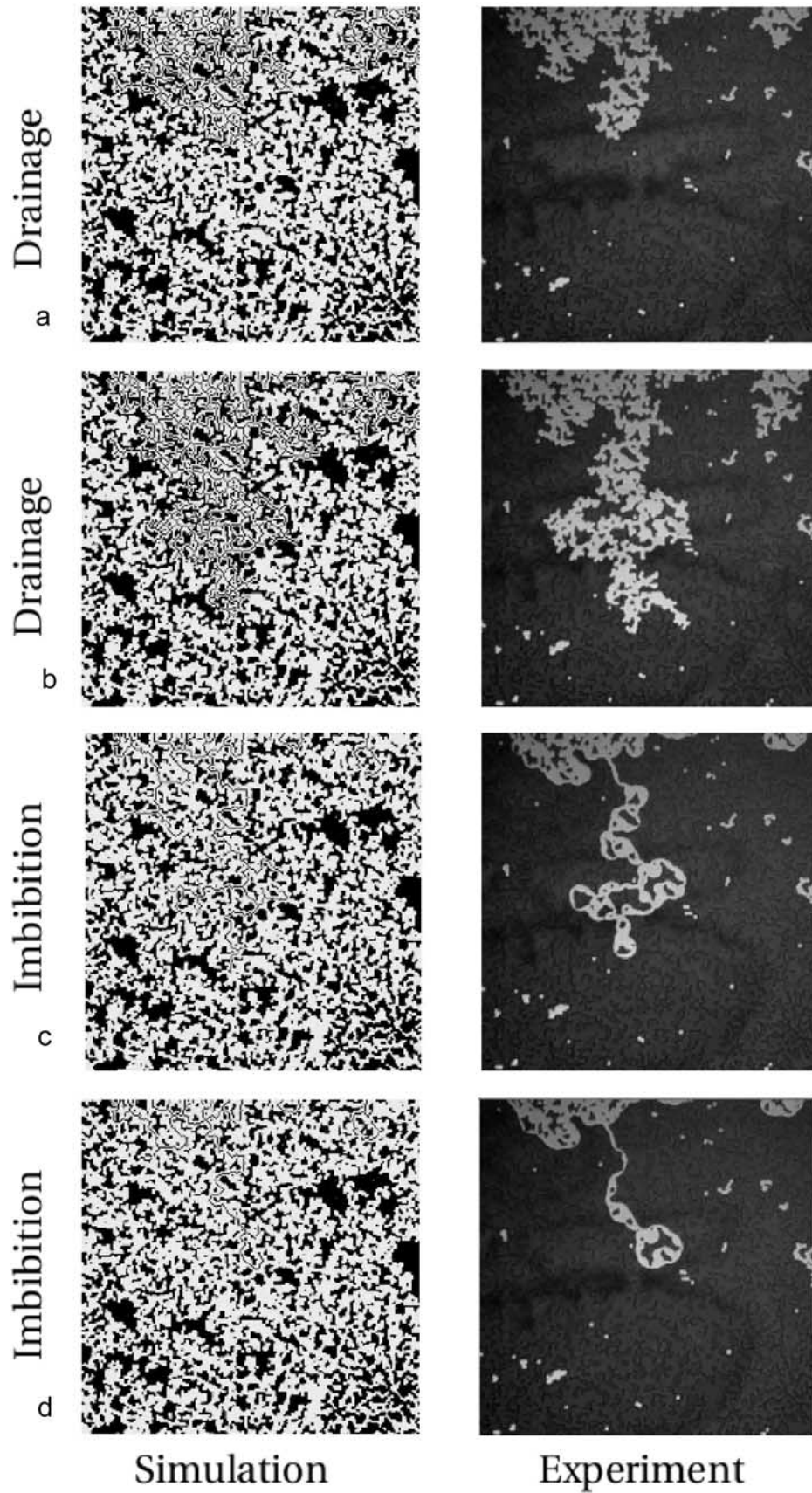


**Figure 8.** Snapshots of the drainage and imbibition experiments, comparison between experiments and simulations. (a and b) Drainage results for snapshots 1 and 2, respectively. (c and d) Imbibition results for snapshots 1 and 2, respectively.

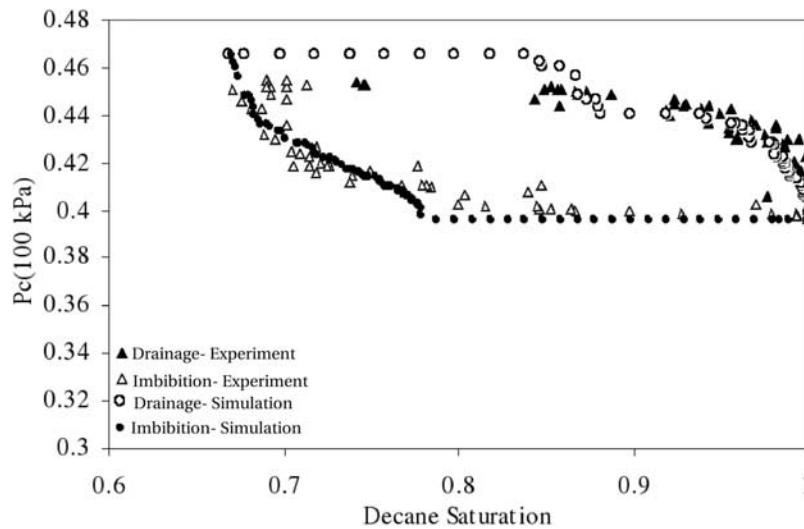


Figure 9. Measured and simulated  $P_c$ - $S$  data points for drainage and imbibition.

imposed. At the end of imbibition, the drainage simulation was repeated. We always obtained only the primary drainage curve because at the end of each imbibition cycle the nonwetting phase has completely exited the micromodel.

#### 4. Results and Discussion

##### 4.1. Network Analysis

[19] Because the depth of the micromodel was constant, a planar pore size distribution was used to analyze the  $P_c$ - $S$  curve behavior. Figure 6 shows the histogram of pore widths assigned to the medial pixels of the image of the micromodel. For a rectangular cross section, equation (1) gives the corresponding entry pressure as a function of the pore width. The resulting curve is plotted in Figure 7. For pore widths larger than  $7 \mu\text{m}$ , only small changes in the entry capillary pressure are required to invade the nonwetting phase into large pore widths because the depth of

the micromodel (pore height, which controls the entry capillary pressure) is constant.

##### 4.2. Fluids Distribution Snapshots

[20] In Figure 8, snapshots of fluid distributions for different saturations from the micromodel experiments and the corresponding network simulations are shown for comparison. The simulations are based on the no-trapping assumption. Figures 8a and 8b show drainage results and Figures 8c and 8d show imbibition results. We observe that the simulated fluid distributions qualitatively agree with the experimentally measured fluid configurations. Cooperative filling of the pores appears to dominate the fluid configurations in this micromodel.

##### 4.3. $P_c$ - $S$ Curves

[21] In Figure 9, we compared  $P_c$ - $S$  curves for drainage and imbibition obtained from our simulations with the measured curves from the micromodel experiments. Good

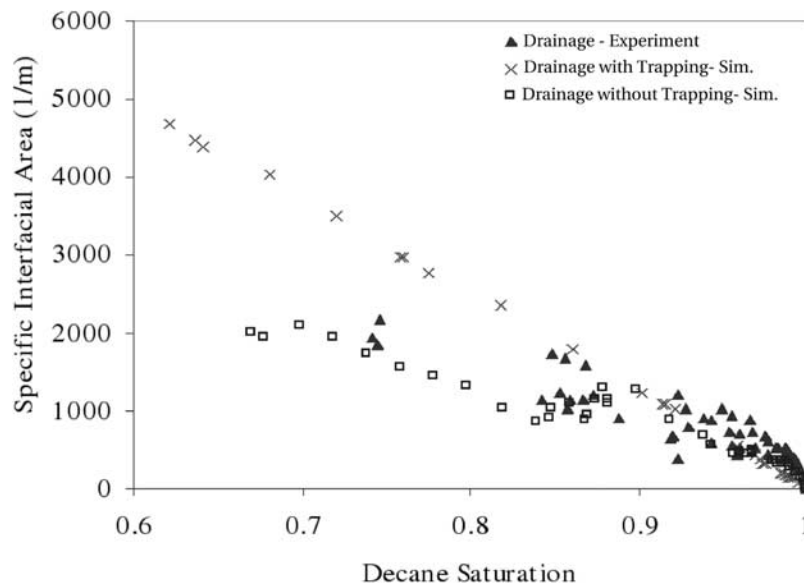
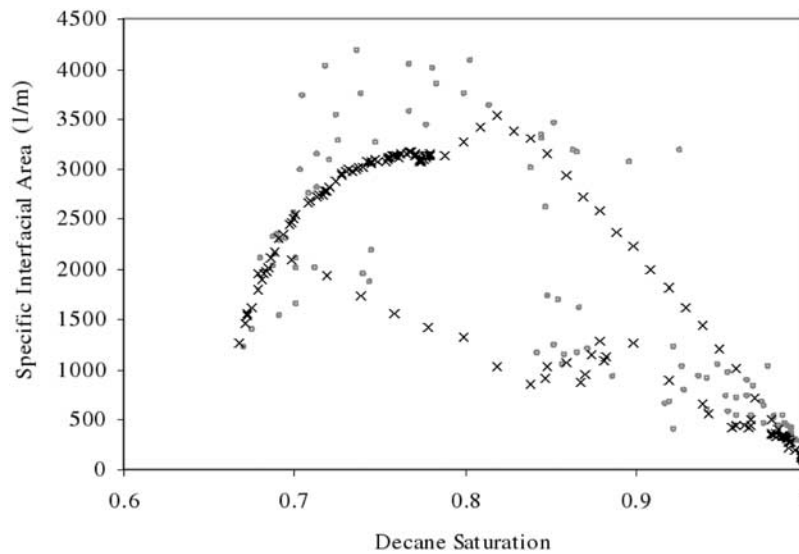


Figure 10. The  $a_{mw}$ - $S$  points resulted from drainage experiments and simulations.



**Figure 11.** Experimental and computational  $a_{nw}$ - $S$  relationship for drainage and imbibition (circles show experiment data, and crosses show simulation data). Interfacial area during drainage is much less than during imbibition.

agreement between the experimental data and the numerical simulations was obtained. It is interesting to note that portions of both the drainage and imbibition curves are flat. During drainage for saturations less than 0.83, the  $P_c$ - $S$  curve are almost flat. This flat shape of the capillary pressure is caused by the spatial distribution of the micromodel pores. Pore constrictions act as bottlenecks that prevent the nonwetting phase from further invading the micromodel until the capillary pressure is high enough to breakthrough the bottleneck pore. After invading the bottleneck, a large region of the pore space is flooded at almost constant capillary pressure. Because of the absence of a hydrophilic membrane, breakthrough of nonwetting phase occurs at a relatively high saturation. This also means that the imbibition curve is not the main imbibition curve but a scanning curve. The flat part of the imbibition curve occurs above a saturation of 0.78. At this saturation, flooding of the micromodel by the wetting phase occurred at an almost constant capillary pressure of 39 kPa. This is the capillary pressure that corresponds to a meniscus with radius 1.28  $\mu\text{m}$ , i.e., the depth of micromodel.

#### 4.4. The $a_{nw}$ - $S$ Relationship

[22] In Figure 10,  $a_{nw}$ - $S$  data points obtained from the pore network model are compared to the measured  $a_{nw}$ - $S$  data. As mentioned earlier, pore network computations can be performed with two scenarios: with or without trapping. The effect of these two scenarios on the  $a_{nw}$ - $S$  relationship is shown in Figure 9. The points obtained from the no-trapping scenario are in good agreement with the experimental measurements. This indicates that the no-trapping assumption is valid for drainage. The  $a_{nw}$ - $S$  curves were also calculated for many cycles of drainage and imbibition, invoking the no-trapping assumption for drainage and the forced displacement assumption for imbibition. The result is shown in Figure 11. Interfacial area is underestimated by the simulations for imbibition. We hypothesize that this is caused by not accounting for

the cooperative filling that occurs during imbibition. Interfaces that span a number of pores (Figure 1) have a larger interfacial area than the interfaces that are confined within a single pore.

#### 4.5. $P_c$ - $S$ - $a_{nw}$ Surface

[23] Several researchers have computationally generated  $P_c$ - $S$ - $a_{nw}$  surfaces for either drainage or imbibition in lattice networks [Reeves and Celia, 1996; Held and Celia, 2001; Joekar-Niasar et al., 2008] to investigate Hassanizadeh and Gray [1990] conjecture that capillary pressure is not only a function of saturation, but also of interfacial area between nonwetting and wetting phases. In this paper, we produce a  $P_c$ - $S$ - $a_{nw}$  surface using both the main drainage curve and the imbibition scanning curves. A second-order polynomial surface was fitted separately to the experimental data and to the simulation data. A high correlation between the fitted surface and data was observed that corresponded to correlation coefficients for the simulations and experiments of 0.99 and 0.95, respectively. It has been observed that there are some fluctuations in the experimental data points, due to limitation in resolution of image acquisition and accuracy of pressure transducer. Using interpolation, a map of interfacial distribution within the  $P_c$ - $S$  loop is obtained and is shown in Figure 12 for both simulations (Figure 12a) and experimental data (Figure 12b). We then subtracted these two maps to obtain a map of normalized differences (Figure 12c). The average normalized difference is 0.17 and it is larger only in a very small range at high saturations (0.97 to 1.00), where the magnitude of interfacial area is small. On the basis of the analysis done on interfacial area, it can be concluded that we have been able to define a single descriptive surface for the imbibition curves that also includes the main drainage curve. This conclusion is similar to that found experimentally by Chen et al. [2007]. They showed experimentally that the  $P_c$ - $S$ - $a_{nw}$  surfaces obtained for drainage and imbibition were the same to within the experimental and analysis error (around 10–15%). Our computational results and the work of Chen et al. [2007] suggest that data obtained from either

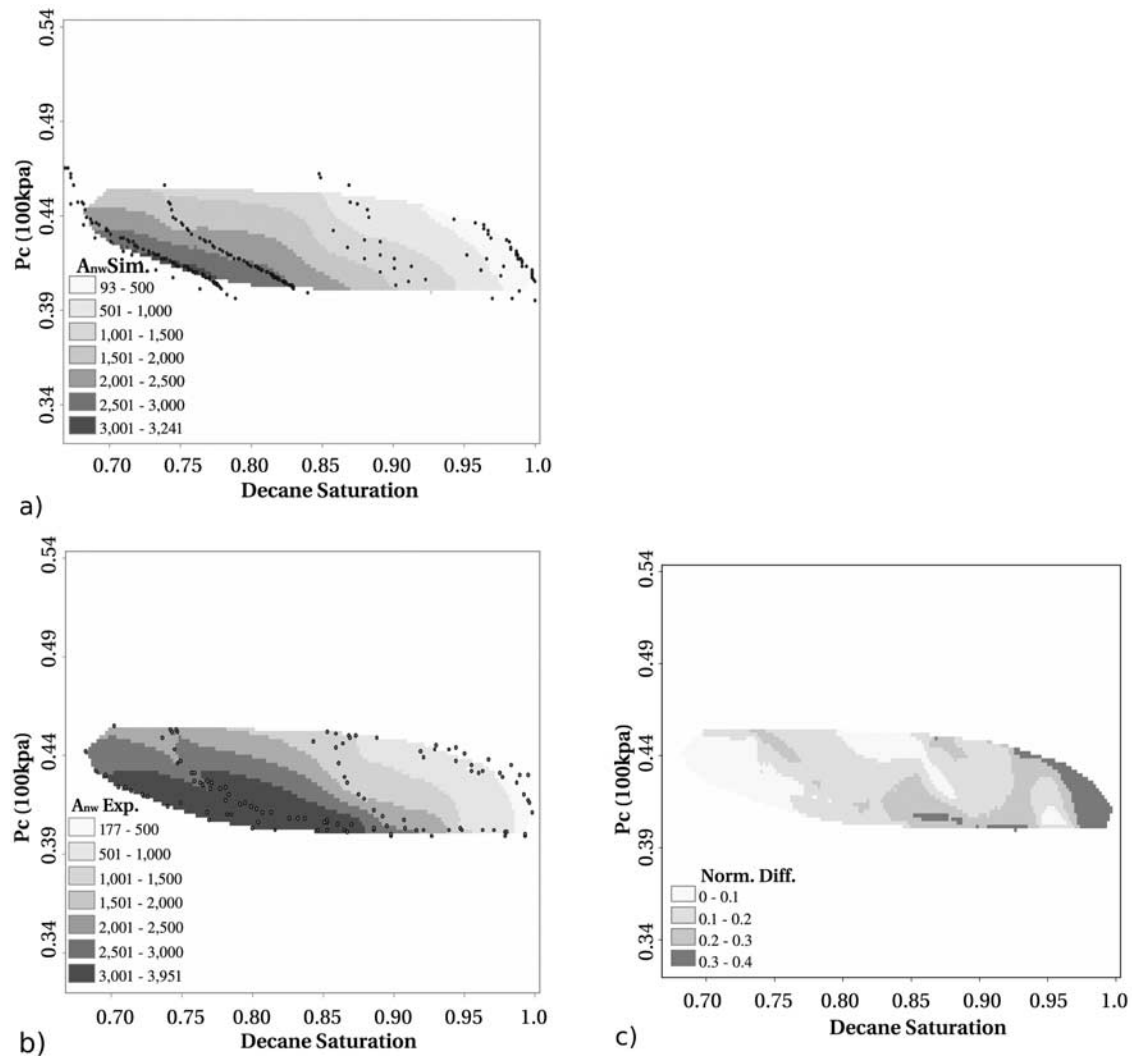


**Figure 12.** Spatial distribution of specific interfacial area (1/m) for (a) simulations, (b) experiments, and (c) normalized differences between Figures 12a and 12b.

the drainage process or the imbibition process are sufficient to generate the complete functional relationship among  $P_c$ - $S_w$ - $a_{nw}$ .

## 5. Summary and Conclusion

[24] In this work, an unstructured pore network model was developed to simulate the drainage and imbibition experiments performed on a two-dimensional micromodel of a porous medium to produce  $P_c$ - $S$ - $a_{nw}$  surface. Development of the pore network model was based on identifying the medial pixels of a pixelized image of the pore space in the micromodel. We have employed a simple approach based on distance transform (DT) to define medial pixels. Using this concept, geometry and topology of the micromodel are captured with an acceptable accuracy for use in a pore network model. We have demonstrated the capability of the model by simulating the configuration of two immiscible fluids in a micromodel. Our analysis shows that capillary pressure of the micromodel is controlled by its depth, which is almost as small as the smallest pore width. In addition, the spatial distribution

of pores with variable widths is such that a constriction (i.e., a bottleneck) controls the invasion of the nonwetting (i.e., a bottleneck) controls the invasion of the nonwetting phase to a significant portion of the micromodel. Because of the rectangular cross section of the pores, no trapping of the wetting phase occurred during drainage. The wetting phase in the corners of invaded pores of the network was always connected to the outflow reservoir. This conclusion was checked by comparing the computationally obtained  $a_{nw}$ - $S$  relationship for different assumptions to the  $a_{nw}$ - $S$  relationship from the experiments. If there is trapping,  $a_{nw}$  would be monotonically increasing with decreasing saturation. However, if there is no trapping, the  $a_{nw}$ - $S$  curve is parabolic in shape with a maximum value at an intermediate saturation [e.g., Joekar-Niasar et al., 2008]. The  $a_{nw}$ - $S$  curve from the micromodel experiments had a parabolic shape, which confirms that no trapping occurred in micromodel drainage experiments. Finally using our pore network model, we reproduced the observed patterns of fluid distribution in the micromodel for both drainage and imbibitions experiments. We also produced a  $P_c$ - $S$ - $a_{nw}$  surface for imbibition that approximated the measured

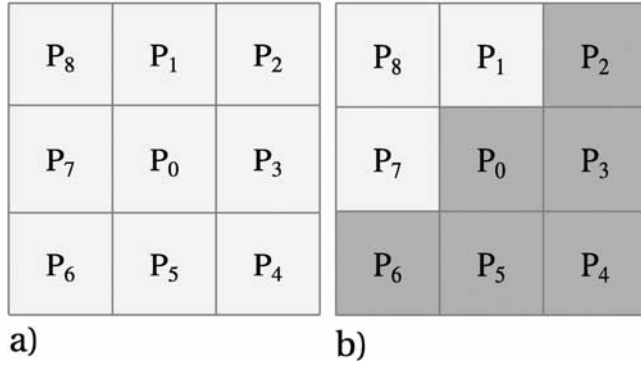


**Figure A1.** Definition of a boundary pixel, (a)  $P_0^\alpha$  is not a boundary pixel  $|\mathbb{N}_i^\alpha| = 8$ ; (b)  $P_0^\alpha$  is a boundary pixel,  $|\mathbb{N}_i^\alpha| = 5 < 8$ ; shading shows the arbitrary phases.

surface very closely. This is very encouraging as it suggests that we can use our pore network model as a predictive tool.

### Appendix A: Determination of Medial Pixels

[25] Our approach for identifying medial pixels is explained in three parts. First, the micromodel domain decomposition is introduced. Then, the distance transform (DT) is explained, and finally a flow operator, which is used for determining the medial pixels, is covered.

#### A1. Micromodel Domain Decomposition

[26] Let  $\Omega_t \in \mathbb{R}^2$  include all pixels existing in the micromodel domain including solid domain  $\Omega_s \in \mathbb{R}^2$  and void domain  $\Omega_v \in \mathbb{R}^2$ . Void domain can include two different phase domains: nonwetting phase  $\Omega_{nw} \in \mathbb{R}^2$  and wetting phase  $\Omega_w \in \mathbb{R}^2$ . Thus, we may write

$$\Omega_v := \Omega_{nw} \cup \Omega_w \quad (\text{A1})$$

$$\Omega_t := \Omega_v \cup \Omega_s := \Omega_{nw} \cup \Omega_w \cup \Omega_s \quad (\text{A2})$$

As a short-hand notation, we can write  $\Omega_i := \cup \Omega_\alpha : \alpha = w, nw, s$ . Each pixel  $i$ , shown as  $P_i^\alpha$ , belongs to a domain  $\alpha$ . In a two-dimensional domain,  $P_i^\alpha$  can have a maximum of eight neighbors which belong to domain  $\alpha$ . The set of those pixels neighboring  $P_i^\alpha$  and belonging to the domain  $\alpha$ , is denoted by  $\mathbb{N}_i^\alpha$ . In addition, total number of elements of set  $\mathbb{N}_i^\alpha$  is denoted by  $|\mathbb{N}_i^\alpha|$ .

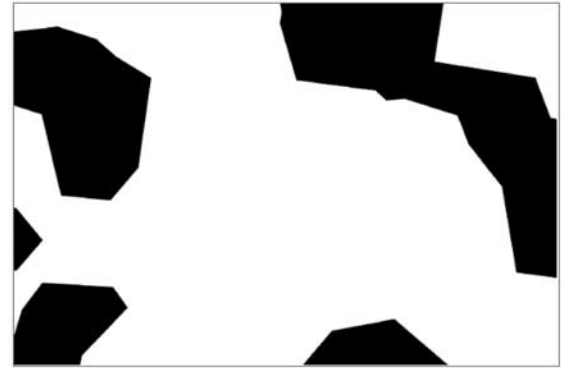
[27] Thus, boundary pixels for the domain  $\alpha$  can be identified as follows:

$$\partial\Omega_\alpha := \{P_i^\alpha \in \Omega_\alpha : |\mathbb{N}_i^\alpha| < 8\}, \quad \alpha = nw, w, s \quad (\text{A3})$$

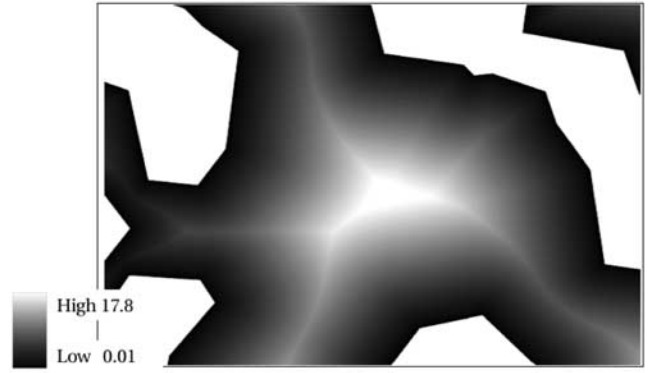
For example, pixel  $P_0$  is not a boundary pixel in Figure A1a, but in Figure A1b it is a boundary pixel.

#### A2. Distance Transform

[28] Let the Euclidean distance between the centers of two pixels  $P_i^\alpha$  and  $P_j^\alpha$  be denoted by  $d(P_i^\alpha, P_j^\alpha)$ . Distance transform, DT, is calculated as the minimum Euclidean



a)



b)

**Figure A2.** (a) Binary presentation of a porous medium, black is the solid domain and white is the void domain. (b) Spatial distribution of the distance transform.

distance between the center of a pixel in the void domain and pixels of solid boundary.

$$DT(P_i^v) = \min\{d(P_i^v, P_j^s) : \forall P_j^s \in \partial\Omega_s\} \quad (\text{A4})$$

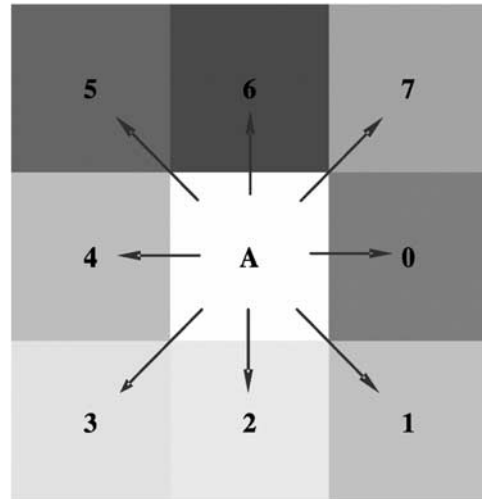


**Figure A3.** Direction numbering for flow operator; the same shading code is used in Figure A4 and A5.

index	1	2	3	4	5	6	7	8	9
1	13.37	13.28	13.20	13.08	12.88	12.69	12.52	12.35	12.20
2	13.77	13.68	13.60	13.43	13.24	13.06	12.89	12.73	12.58
3	14.16	14.08	13.98	13.79	13.60	13.42	13.26	13.10	12.96
4	14.16	14.08	13.98	13.87	13.77	13.68	13.59	13.48	13.34
5	13.77	13.68	13.59	13.48	13.37	13.28	13.20	13.09	12.98
6	13.37	13.28	13.20	13.09	12.98	12.89	12.80	12.70	12.59
7	12.98	12.89	12.80	12.70	12.59	12.49	12.41	12.31	12.20

a)

index	1	2	3	4	5	6	7	8	9
1	6	6	6	7	7	7	7	7	6
2	6	6	6	7	7	7	7	6	6
3	6	6	7	7	7	7	7	6	6
4	2	2	2	2	2	2	2	2	6
5	2	2	2	2	2	2	2	2	2
6	2	2	2	2	2	2	2	2	2
7	2	2	2	2	2	2	2	2	2

b)

**Figure A4.** (a) An example spatial distribution of distance transform. (b) Result of flow operator based on distribution in Figure A4a.

Result of distance transformation for a given void domain (e.g., Figure A2a) will be a distance map as shown in Figure A2b. In Figure A2b, pixels with a larger distance from the nearest solid boundary pixels are shown in a brighter color.

**A3. Flow Operator**

[29] Within the distance map, each pixel located in the void domain will have a distance value larger than zero. If we assign this value as the height of that pixel, we can create a mountain chain. The ridge of mountain chain is the locus of pixels with the largest DT value (i.e., the largest

distance from solid boundary). To determine pixels located on the ridge, a flow operator is defined. Flow operator, **F**, is used to determine the direction (DIR) of maximum downward slope between the centers of a pixel and its neighboring pixels [Jensen and Domingue, 1988]. Since each pixel of void domain has at most eight neighbors in the void domain, there will be a maximum of eight possible directions as shown in Figure A3. Flow operator can be written as follows:

$$F(P_i^v) = \text{DIR} \left( \max \left\{ \frac{DT(P_i^v) - DT(P_j^v)}{d(P_i^v - P_j^v)} : j \in \mathbb{N}_i^v \right\} \right) \quad (\text{A5})$$

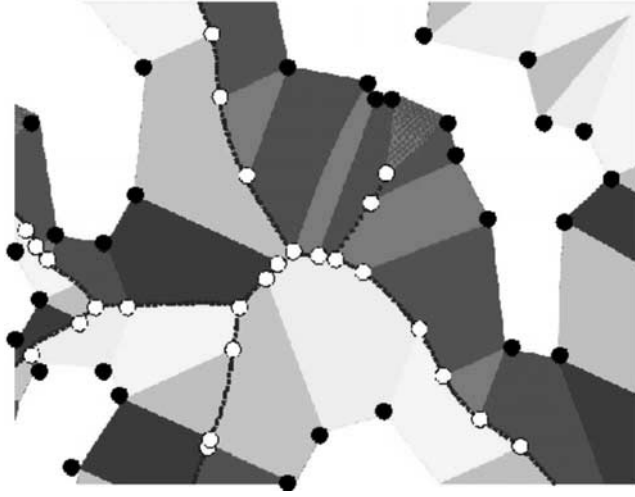


**Figure A5.** Result of flow operator for domain presented in Figure A2, dashed path represents medial path required for the simulation. Solid circles show those cluster boundary pixels, neighboring solid domain pixels. Open circles show those cluster boundary pixels, where at least three different clusters are neighboring each other.

Let the complete set of  $\mathbf{F}(P_i^v)$  consisting of nonrepeating members be denoted by  $\mathbb{F} = \{0, 1, 2, 3, 4, 5, 6, 7\}$  and its cardinality,  $|\mathbb{F}|$ , is of maximum eight. For example, Figure A4b shows the flow operator implemented on a hypothetical distance map presented in Figure A4a. In Figure A4b, pixel (4,2), for example, has three different types of neighbors, namely, 2, 6, and 7; thus  $\mathbb{F}_{(4,2)} = \{2,6,7\}$  and  $|\mathbb{F}_{(4,2)}| = 3$ .

[30] All pixels with a common flow direction form a direction cluster; e.g., there are four direction clusters in Figure A4b, each designated with its own shading. This shading code is used in examples shown in Figures A3 to A5. Thus, flow operator,  $\mathbf{F}$ , creates direction clusters (i.e., clusters of pixels with a common flow direction). Each cluster will be bounded by its boundary pixels. These pixels may see solid boundary pixels in their neighboring cells (e.g., solid circles in Figure A5) or may see more than one type of other clusters in their neighboring cells (e.g., open circles in Figure A5). Finally, using a search algorithm, it is possible to find the medial pixels (e.g., the dashed path crossing through the open circles in Figure A5).

[31] Because of the variability of the pore width in the domain, image analysis should be done at such a resolution that pixel size is smaller than the minimum pore width. The finer the discretization of the domain is, the more precise the pore network will be. In our study, each pixel has a size of  $0.3 \mu\text{m}$ . Sensitivity analysis, based on the  $P_c$ - $S$  curves has shown that this resolution is in acceptable range for generation of the pore network model.

## Appendix B: Calculation of Entry Capillary Pressure for a Rectangular Cross Section

[32] In this appendix, the equation for entry capillary pressure of a tube with rectangular cross section is derived. The approach followed here has been already employed by Mayer and Stowe [1965]; Princen [1969a, 1969b] and Ma et al. [1996] for equilateral polygonal cross sections. When

the nonwetting phase invades the tube, it will be filling the inner part of the tube, with corners filled with the wetting phase as shown in Figure 3. A cross section diagonally along the tube (section F-F in Figure 3) at the moment of invasion is shown in Figure B1. As shown there, the longitudinal curvature of the fluid-fluid interface changes sign just inside the tube; at section G-G; i.e., its curvature in the direction of the tube length is zero. In the cross-sectional direction, its radius of curvature is denoted by  $r_c$ , as shown in Figure 3. Thus, the entry capillary pressure is equal to

$$P_e = P^n - P^w = \frac{\sigma_{nw}}{r_c} \quad (\text{B1})$$

in which,  $P^n$  is pressure of the nonwetting phase, and  $P^w$  is the pressure of the wetting phase. The balance of forces for the interface hanging below the G-G level (in Figure B1) is as follows:

$$(P^n - P^w)A_{nw,eff} = L_{nw}\sigma_{nw} + L_{ns}\sigma_{ns} - L_{ns}\sigma_{ws} \quad (\text{B2})$$

where  $A_{nw,eff}$  is that part of a cross section filled with nonwetting phase,  $L_{ns}$  is the total length of solid-fluid-fluid contact line,  $L_{nw}$  is the total length of arc cut through the fluid-fluid interface in the corners.

[33] From Young equation, we have

$$\sigma_{ns} = \sigma_{nw} \cos \theta + \sigma_{ws} \quad (\text{B3})$$

Substituting equation (B3) in equation (B2) will result in

$$(P^n - P^w)A_{nw,eff} = \sigma_{nw}(L_{nw} + L_{ns} \cos \theta) \quad (\text{B4})$$

Once again, at the entry of the tube by the nonwetting phase, we have  $P_e = P^n - P^w$ . Combination of equations (B1) and (B4) results in

$$\frac{L_{nw} + L_{ns} \cos \theta}{A_{nw,eff}} = \frac{1}{r_c} \quad (\text{B5})$$

Figure 3 shows that corner angle is  $\pi/2$  and contact angle is  $\theta$ . Considering the half corner angle as shown in Figure 3, we can write the following geometrical relations:

$$AH = \sqrt{2} \cos(\pi/4 + \theta)r_c \quad (\text{B6})$$

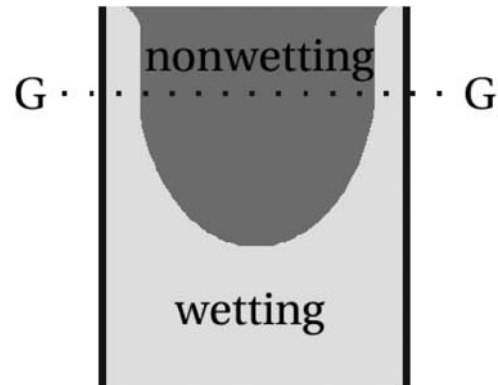


**Figure B1.** Longitudinal section (along F-F in Figure 3) showing nonwetting at the moment of invasion into the tube.

To calculate the area covered by the nonwetting phase,  $A_{nw,eff}$ , we need to substitute the areas of the four corners filled by the wetting phase for the rectangular area,  $ab$ , First, area of half corner triangle will be

$$s_{\Delta AHO} = \left(\sqrt{2}/2\right)r_c^2 \cos(\pi/4 + \theta) \cos \theta \quad (B7)$$

Area of  $ANH$  is calculated as follows:

$$S_{AHN} = \left(\sqrt{2}/2\right)r_c^2 \cos(\pi/4 + \theta) \cos \theta - 0.5r_c^2(\pi/4 - \theta) \quad (B8)$$

[34] Considering the total area of a rectangular,  $S = ab$ , total area of nonwetting fluid is

$$A_{nw,eff} = ab - 4r_c^2 \left[ \sqrt{2} \cos(\pi/4 + \theta) \cos \theta - (\pi/4 - \theta) \right] \quad (B9)$$

In addition, we will have

$$L_{nw} = 8r_c(\pi/4 - \theta) \quad (B10)$$

$$L_{ns} = 2(a + b) - 8\sqrt{2} \cos(\pi/4 + \theta)r_c \quad (B11)$$

Substituting equations (B9), (B10) and (B11) into equation (B5) will result in

$$\frac{8(\pi/4 - \theta)r_c + [2(a + b) - 8\sqrt{2} \cos(\pi/4 + \theta)r_c] \cos \theta}{ab - 4r_c^2 [\sqrt{2} \cos(\pi/4 + \theta) \cos \theta - (\pi/4 - \theta)]} = \frac{1}{r_c} \quad (B12)$$

Equation (12) can be solved for  $r_c$  to obtain

$$r_c = \frac{-(a + b) \cos \theta + \sqrt{(a + b)^2 \cos^2 \theta + 4ab \left[ \frac{\pi}{4} - \theta - \sqrt{2} \cos \left( \frac{\pi}{4} + \theta \right) \cos \theta \right]}}{4 \left[ \frac{\pi}{4} - \theta - \sqrt{2} \cos \left( \frac{\pi}{4} + \theta \right) \cos \theta \right]} \quad (B13)$$

Finally, entry capillary pressure can be calculated using equations (B1) and (B13).

[35] **Acknowledgments.** The authors would like to thank A. Leijnse from Wageningen University for fruitful discussions. Also we are grateful to the anonymous reviewers for their valuable comments. L.J.P.N. wishes to acknowledge the work supported by the National Science Foundation under grant EAR-0509759. Authors are members of the International Research Training Group NUPUS, financed by the German Research Foundation (DFG) and The Netherlands Organization for Scientific Research (NWO).

## References

- Al-Raoush, R. I., and C. S. Willson (2005a), Extraction of physically realistic pore network properties from three-dimensional synchrotron x-ray microtomography images of unconsolidated porous media systems, *J. Hydrol.*, *300*, 44–64.
- Al-Raoush, R. I., and C. S. Willson (2005b), A pore-scale investigation of a multiphase porous media system, *J. Contam. Hydrol.*, *77*, 67–89.
- Blum, H. (1967), A transformation for extracting new descriptors of shape, in *Models for the Perception of Speech and Visual Form*, edited by W. Wathen-Dun, pp. 362–380, MIT Press, Cambridge, Mass.
- Blunt, M., M. D. Jackson, M. Piri, and P. H. Valvatne (2002), Detailed physics, predictive capabilities and macroscopic consequences for pore-network models of multiphase flow, *Adv. Water Resour.*, *25*, 1069–1089.
- Brady, M., and H. Asada (1984), Smoothed local symmetries and their implementation, *Int. J. Robotics Res.*, *3*, 36–61.

- Chandran, S., S. K. Kim, and D. M. Mount (1992), Parallel computational geometry of rectangles, *Algorithmica*, *7*, 25–49.
- Chang, F., Y. C. Lu, and T. Pavlidis (1999), Feature analysis using line sweep thinning algorithm, *IEEE Trans. Pattern Anal. Mach. Intell.*, *21*, 145–158.
- Chatzis, I., and F. A. L. Dullien (1981), Mercury porosimetry curves of sandstones, mechanisms of mercury penetration and withdrawal, *Powder Technol.*, *29*, 117–125.
- Chen, D. Q., L. J. Pyrak-Nolte, J. Griffin, and N. J. Giordano (2007), Measurement of interfacial area per volume for drainage and imbibition, *Water Resour. Res.*, *43*, W12504, doi:10.1029/2007WR006021.
- Cheng, J. T. (2002), Fluid flow in ultra-small structures, Ph.D. thesis, Purdue Univ., West Lafayette, Indiana.
- Cheng, J. T., L. J. Pyrak-Nolte, and D. D. Nolte (2004), Linking pressure and saturation through interfacial area in porous media, *Geophys. Res. Lett.*, *31*, L08502, doi:10.1029/2003GL019282.
- Coles, M. E., et al. (1998), Developments in synchrotron x-ray microtomography with applications to flow in porous media, *SPE Reservoir Eval. Eng.*, *1*, 288–296.
- Culligan, K. A., D. Wildenschild, B. S. B. Christensen, W. Gray, M. L. Rivers, and A. F. B. Tompson (2004), Interfacial area measurements for unsaturated flow through a porous medium, *Water Resour. Res.*, *40*, W12413, doi:10.1029/2004WR003278.
- Culligan, K. A., D. Wildenschild, B. S. B. Christensen, W. Gray, M. L. Rivers, and A. F. B. Tompson (2006), Pore-scale characteristics of multiphase flow in porous media: A comparison of air–water and oil–water experiments, *Adv. Water Resour.*, *29*, 227–238.
- Dias, M. M., and A. C. Payatakes (1986), Network models for two-phase flow in porous media, part 1. Immiscible microdisplacement of non-wetting fluids, *J. Fluid Mech.*, *164*, 305–336.
- Dubikovskaya, A. A., O. V. Kirichenko, and V. G. Lapshin (1990), High-porosity thin-fiber metallic material, *Mater. Sci.*, *25*, 372–373.
- Fatt, I. (1956), The network model of porous media, I. Capillary pressure characteristics, *Petroleum Trans. AIME*, *207*, 144–159.
- Fredrich, J. T., K. H. Greaves, and J. W. Martin (1993), Pore geometry and transport-properties of Fontainebleau sandstone, *Int. J. Rock Mech. Min. Sci. Geomech. Abstr.*, *30*, 691–697.
- Fredrich, J. T., B. Menendez, and T. F. Wong (1995), Imaging the pore structure of geomaterials, *Science*, *268*, 276–279.
- Glantz, R., and M. Hilpert (2007), Dual models of pore spaces, *Adv. Water Resour.*, *30*, 227–248.
- Glantz, R., and M. Hilpert (2008), Tight dual models of pore spaces, *Adv. Water Resour.*, *31*, 787–806.
- Hassanizadeh, S. M., and W. G. Gray (1990), Mechanics and thermodynamics of multiphase flow in porous media including interphase boundaries, *Adv. Water Resour.*, *13*, 169–186.
- Held, R. J., and M. A. Celia (2001), Modeling support of functional relationships between capillary pressure, saturation, interfacial area and common lines, *Adv. Water Resour.*, *24*, 325–343.
- Ioannidis, M. A., I. Chatzis, and A. C. Payatakes (1991), A mercury porosimeter for investigating capillary phenomena and microdisplacement mechanisms in capillary networks, *J. Colloid Interface Sci.*, *143*, 22–36.
- Jensen, S. K., and J. O. Domingue (1988), Extracting topographic structure from digital elevation data for geographic information system analysis, *Photogramm. Eng. Remote Sens.*, *54*, 1593–1600.
- Joekar-Niasar, V., S. M. Hassanizadeh, and A. Leijnse (2008), Insights into the relationships among capillary pressure, saturation, interfacial area and relative permeability using pore-network modeling, *Transp. Porous Media*, *74*, 201–219.
- Knackstedt, M., C. Arns, A. Limaye, A. Sakellariou, T. Senden, A. Sheppard, R. Sok, W. Pinczewski, and G. Bunn (2004), Digital core laboratory: properties of reservoir core derived from 3D images, *J. Pet. Technol.*, *56*, 66–68.
- Lam, L., and S. W. Lee (1992), Thinning methodologies—a comprehensive survey, *IEEE Trans. Pattern Anal. Mach. Intell.*, *14*, 869–885.
- Lee, D. T. (1982), Medial axis transformation of a planar shape, *IEEE Trans. Pattern Anal. Mach. Intell.*, *4*, 363–369.
- Lenormand, R., and C. Zarcone (1983), Mechanism of the displacement of one fluid by another in a network of capillary ducts, *J. Fluid Mech.*, *135*, 337–353.
- Lenormand, R., and C. Zarcone (1984), Role of roughness and edges during imbibition in square capillaries, SPE paper 13264 presented at 59th Annual Technical Conference of the Houston SPE, Richardson, Tex.
- Lindquist, W. B. (2002), Network flow model studies and 3d pore structure, *Contemp. Math.*, *295*, 355–366.
- Lindquist, W. B., A. Venkatarangan, J. Dunsmuir, and T. F. Wong (2000), Pore and throat size distributions measured from synchrotron X-ray tomography

- graphic images of Fontainebleau sandstones, *J. Geophys. Res.*, *105*, 21,508–21,528.
- Ma, S., G. Mason, and N. R. Morrow (1996), Effect of contact angle on drainage and imbibition in regular polygonal tubes, *Colloids Surf. A*, *117*, 273–291.
- Mahmud, W. M., and V. H. Nguyen (2006), Effects of snap-off in imbibition in porous media with different spatial correlations, *Transp. Porous Media*, *64*, 279–300.
- Matsuyama, T., and T. Y. Phillips (1984), Digital realization of the labeled Voronoi diagram and its application to closed boundary detection, in *Proceedings of the 7th International Conference on Pattern Recognition*, pp. 478–480, Comput. Soc. Press, New York.
- Mayer, R. P., and R. A. Stowe (1965), Mercury porosimetry-breakthrough pressure for penetration between packed spheres, *J. Colloid Sci.*, *20*, 891–911.
- Montanari, U. (1969), Continuous skeletons from digitized images, *J. ACM*, *16*, 534–549, doi: <http://doi.acm.org/10.1145/321541.321543>.
- Montemagno, C. D., and L. J. Pyrak-Nolte (1995), Porosity of fracture networks, *Geophysical Research Letters*, *22*, 1397–1401.
- Montoto, M., A. Martineznistal, A. Rodriguezrey, N. Fernandezmerayo, and P. Soriano (1995), Microfractography of granitic-rocks under confocal scanning laser microscopy, *J. Microsc. Oxford*, *177*, 138–149.
- Ogniewicz, R., and M. Ilg (1992), Voronoi skeletons: Theory and applications, in *Proceedings CVPR '92, 1992 IEEE Computer Society Conference on Computer Vision and Pattern Recognition*, pp. 63–69, Inst. of Electr. and Electron. Eng., New York.
- Piri, M., and M. J. Blunt (2005a), Three-dimensional mixed-wet random pore-scale network modeling of two- and three-phase flow in porous media. I. Model description, *Phys. Rev. E*, *71*, 026,301.
- Piri, M., and M. J. Blunt (2005b), Three-dimensional mixed-wet random pore-scale network modeling of two- and three-phase flow in porous media. II. Results, *Phys. Rev. E*, *71*, 026,302.
- Princen, H. M. J. (1969a), Capillary phenomena in assemblies of parallel cylinders I. Capillary rise between two cylinders, *Colloid Interface Sci.*, *30*, 69–75.
- Princen, H. M. J. (1969b), Capillary phenomena in assemblies of parallel cylinders II. Capillary rise in systems with more than two cylinders, *Colloid Interface Sci.*, *30*, 359–371.
- Pyrak-Nolte, L. J., D. D. Nolte, D. Q. Chen, and N. J. Giordano (2008), Relating capillary pressure to interfacial areas, *Water Resour. Res.*, *44*, W06408, doi:10.1029/2007WR006434.
- Reeves, P. C., and M. A. Celia (1996), A functional relationship between capillary pressure, saturation, and interfacial area as revealed by a pore-scale network model, *Water Resour. Res.*, *32*, 2345–2358.
- Reimbrecht, E. G., E. Bazzo, L. H. S. Almeida, H. C. Silva, C. Binder, and J. L. R. Muzart (2003), Manufacturing of metallic porous structures to be used in capillary pumping systems, *Mater. Res.*, *6*, 481–486.
- Rosenfeld, A., and J. L. Pfalz (1968), Distance function on digital pictures, *Pattern Recogn.*, *1*, 33–61.
- Saint-Marc, P., H. Rom, and G. Medioni (1993), B-spline contour representation and symmetry detection, *IEEE Trans. Pattern Anal. Mach. Intell.*, *15*, 1191–1197.
- Smith, R. W. (1987), Computer processing of line images: a survey, *Pattern Recogn.*, *20*, 7–15.
- Valvatne, P. H., and M. J. Blunt (2004), Predictive pore-scale modeling of two-phase flow in mixed wet media, *Water Resour. Res.*, *40*, W07406, doi:10.1029/2003WR002627.
- Vidales, A. M., J. L. Riccardo, and G. Zgrabli (1998), Pore-level modelling of wetting on correlated porous media, *J. Phys. D, Appl. Phys.*, *31*, 2861–2868.
- Vogel, H. J. (1997), Morphological determination of pore connectivity as a function of pore size using serial sections, *Eur. J. Soil Sci.*, *48*, 365–377.
- Vogel, H. J. (2000), A numerical experiment on pore size, pore connectivity, water retention, permeability, and solute transport using network models, *Eur. J. Soil Sci.*, *51*, 99–105.
- Vogel, H. J., and K. Roth (1998), A new approach for determining effective soil hydraulic functions, *Eur. J. Soil Sci.*, *49*, 547–556.
- Wardlaw, N. C., and L. Yu (1988), Fluid topology, pore size and aspect ratio during imbibition, *Transp. Porous Media*, *3*, 17–34.
- Wildenschild, D., J. W. Hopmans, C. M. P. Vaz, M. L. Rivers, and D. Rikard (2002), Using X-ray computed tomography in hydrology: Systems, resolutions, and limitations, *J. Hydrol.*, *267*, 285–297.
- Wu, A. Y., S. K. Bhaskar, and A. Rosenfeld (1986), Computation of geometric properties from the medial axis transform in time, *Comput. Vision Graph. Image Process.*, *34*, 76–92.
- Wu, A. Y., S. K. Bhaskar, and A. Rosenfeld (1988), Parallel computation of geometric properties from the medial axis transform, *Comput. Vision Graph. Image Process.*, *41*, 323–332.
- Ye, Q. Z. (1988), The signed Euclidean distance transform and its applications, in *Proceedings of the 9th International Conference on Pattern Recognition*, pp. 495–499, Comput. Soc. Press, New York, doi:10.1109/ICPR.1988.28276.

---

C. Berentsen, Department of Geotechnology, Technical University of Delft, Stevinweg 1, Delft, NL-2628 CN, Netherlands.

S. M. Hassanzadeh and V. Joekar Niasar, Department of Earth Sciences, Utrecht University, P.O. Box 80021, Utrecht, NL-3508 TA, Netherlands. (joekar@geo.uu.nl)

L. J. Pyrak-Nolte, Department of Physics, Purdue University, 525 Northwestern Avenue, West Lafayette, IN 47907-2036, USA.